SmallMinesDS: A Multimodal Dataset for Mapping Artisanal and Small-Scale Gold Mines

Stella Ofori-Ampofo, Antony Zappacosta, Rıdvan Salih Kuzu, Peter Schauer, Martin Willberg, and Xiao Xiang Zhu, *Fellow, IEEE*

***Abstract*— The increasing demand for gold, coupled with persistently high market prices over the past decade, has driven a significant rise in small-scale gold production. The expansion of unregularized small-scale gold mines fuels environmental degradation and poses a risk to miners and mining communities. To promote sustainable mining practices, support reclamation initiatives, and pave the way for understudying the impacts of mining on human and environmental resources, we present *SmallMinesDS*, a benchmark dataset derived from multisensor satellite imagery covering five districts in southwestern Ghana in two time periods. *SmallMinesDS* provides precise reference data for artisanal mining sites, enabling the development of machine learning models for timely, large-scale, and cost-effective monitoring. Notably, foundation models (FMs) fine-tuned on *SmallMinesDS* achieve up to 75% intersection over union while maintaining a strong balance between minimizing false positives and negatives.**

***Index Terms*— Earth observation, foundation models (FMs), machine learning, mining, semantic segmentation.**

I. Introduction

ARTISANAL and small-scale gold mining (ASGM) is the primary livelihood for 10–15 million people worldwide [1]. Unlike large-scale mining, ASGM operates on a smaller scale, with distinct regulatory frameworks and socioeconomic impacts. These differences shape how communities engage with and are affected by mining activities.

Central to most ASGM operations is the use of mercury amalgamation for gold extraction [2], a practice responsible for approximately 2000 tons of mercury emissions annually. This makes ASGM the largest source of anthropogenic mercury emissions globally [1]. Beyond mercury emissions, the environmental and health implications are far-reaching, with ASGM linked to deforestation, water pollution, soil degradation, reduced agricultural productivity, economic disruptions, and severe health issues such as kidney dysfunction and neurological disorders [3], [4], [5], [6], [7], [8].

ASGM has a large global presence and is practiced in more than 70 countries [1]. In response, numerous national and international initiatives have been launched to formalize the ASGM sector to promote mercury-free and environmentally sustainable mining practices [9], [10]. These efforts underscore the need for efficient methods to map and monitor ASGM activities to quantify their scale and assess the functioning of interventions to ensure that countries meet their commitment to the Minimata Convention and the realization of sustainable development goals.

Satellite imagery offers a valuable resource for identifying and mapping ASGM activities due to their distinct visual characteristics. The existing studies have predominantly relied on optical or radar imagery to rapidly map the spatial distribution of ASGM using image thresholding [11] and classical machine learning or deep learning approaches [12], [13], [14]. However, these efforts face significant challenges, including the lack of publicly available ASGM labels, which limits reproducibility and broader use by the scientific community and stakeholders. Openly accessible databases of mining areas [15], [16] delineated from satellite basemaps also lack information to indicate acquisition dates, hence limiting their alignment to satellite images and consequently prohibiting their use as labels for machine learning. Furthermore, other accessible datasets only target large-scale mines [17] whose spatial and spectral characteristics differ from ASGM.

Machine learning models used in existing studies for mapping mining sites are often highly specialized, tailored to specific tasks, and do not capitalize on the broader capabilities offered by pretrained or foundation models (FMs). In contrast, FMs offer a more generalized and adaptable approach, learning from large, diverse datasets and providing pretrained baseline that can be fine-tuned for a variety of downstream tasks [18], [19]. This paradigm allows for greater flexibility, improved generalization, and the potential for more robust and scalable ASGM mapping particularly given the geographically dispersed nature of ASGM activities.

In this letter, we present the first version of open-access ASGM labels over southwestern Ghana, marking a pivotal step toward global ASGM mapping. We demonstrate the potential of both the task-specific and geospatial FMs in mapping ASGM sites using satellite imagery. By addressing current

Received 4 February 2025; revised 14 April 2025; accepted 15 April 2025. Date of publication 2 May 2025; date of current version 16 May 2025. This work was supported in part by the FAST-EO Project funded by European Space Agency (ESA) under Contract 4000143501/23/I-DT and in part by the Munich Aerospace e.V. Scholarship. *(Stella Ofori-Ampofo and Antony Zappacosta contributed equally to this work.) (Corresponding author: Rıdvan Salih Kuzu.)*

Stella Ofori-Ampofo and Xiao Xiang Zhu are with the Chair of Data Science in Earth Observation, Technical University of Munich (TUM), 80333 Munich, Germany (e-mail: stella.ofori-ampofo@tum.de; xiaoxiang.zhu@tum.de).

Antony Zappacosta and Rıdvan Salih Kuzu are with the Remote Sensing Technology Institute, German Aerospace Center (DLR), 82234 Wessling, Germany (e-mail: antony.zappacosta@dlr.de; ridvan.kuzu@dlr.de).

Peter Schauer and Martin Willberg are with Industrieanlagen-Betriebsgesellschaft mbH (IABG), 85521 Ottobrunn, Germany (e-mail: schauer@iabg.de; willberg@iabg.de).

Data is available on-line at: https://github.com/DLR-MF-DAS/SmallMinesDS

Digital Object Identifier 10.1109/LGRS.2025.3566356

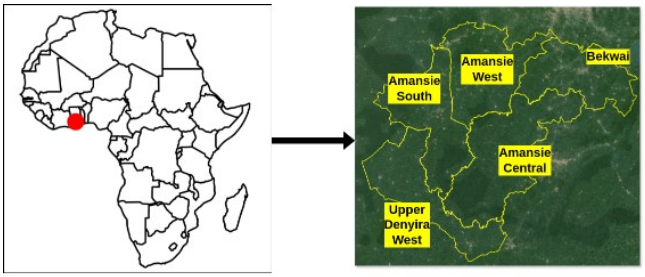

Fig. 1. Map showing the location of the study area in Africa—Ghana (left) and the five districts it covers (right).

limitations and leveraging advanced methodologies, this work lays the foundation for scalable and reproducible ASGM mapping, contributing to the broader objectives of sustainable development and responsible mining practices.

II. SmallMines Dataset

This first version of *SmallMinesDS* covers five administrative districts in southwestern Ghana with a ground area of about 3500 km^2 (see Fig. 1). The study area is ecologically diverse, supporting rich biodiversity and serving as a hub for various land-use activities, including agriculture, forestry, and both industrial and small-scale gold mining. This complex and dynamic landscape of the region mirrors the characteristics of ASGM sites in other parts of the world, highlighting the critical need for accurate mapping and monitoring of ASGM activities. The area is also characterized by two rainfall regimes, which commence around March and September each year. Satellite imagery acquired with optical sensors in this area is often heavily obscured by cloud cover, yielding only a limited number of usable images annually. While radar imagery is less affected by cloud cover and is available throughout the year, its utility during the wet season is compromised by atmospheric interferences caused by intense rainfall events [11]. To facilitate the mapping of ASGM amidst this drawback, *SmallMinesDS* includes dry-season satellite images from both the optical and radar sensors. This strategic selection ensures improved image quality and reliability for analysis.

A. Satellite Data

Artisanal mining sites can be observed in riparian zones, represented as depressions in terrain data. Hence, elevation data can be a useful feature for ML models. Data from the Copernicus Digital Elevation Model [20] are acquired from GEE [21]. The data represent a 10-m digital surface model which includes natural and built features on the Earth's surface. Dry-season Sentinel-1/2 images of January 2016 and 2022 are included in the *SmallMinesDS*. The selection of the base year was due to the earliest cloud-free imagery available for the study area. 10- and 20-m bands of Sentinel-2 surface reflectance images (L2A) are retrieved from the Copernicus Sentinel Data Hub [22]. Consequently, radiometrically terrain-corrected Sentinel-1 images (VV, VH) are acquired from Microsoft Planetary Computer [23] for the same period. To reduce the effect of speckles, a circular mean filter of size 3×3 pixels is applied which also preserves the edges of the circular-like structures of ASGM. The resulting image is converted into dB scale using $10 \times \log 10(x)$.

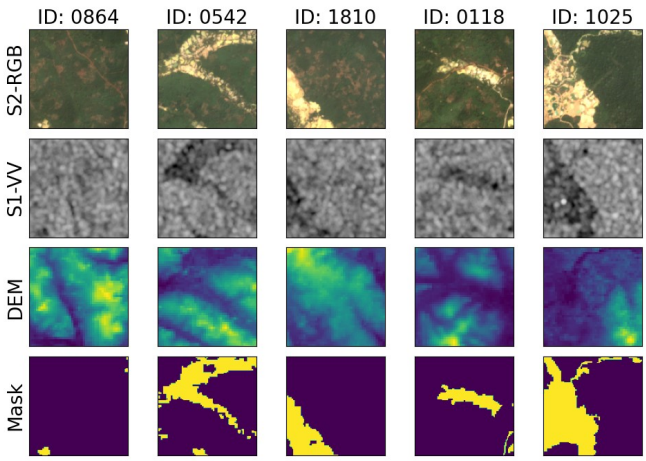

Fig. 2. Sample patches showing ASGM sites as observed from Sentinel-2 RGB, Sentinel-2 VV, and Copernicus DEM.

B. Small-Scale Mining Labels

ASGM sites may look similar to sand-winned regions or settlements with bright roofs when observed in a true-color composite. Their spatial footprint may appear circular and follow the pattern of river networks. To manually create mining labels, Sentinel-2 images for each year are independently segmented using the mean shift algorithm [24]. First, the study area is divided into four geographic blocks, each processed separately to account for potential spatial variations in mining site characteristics and to maintain manageable data sizes. Each block contains approximately one million image segments. About 2% of the segments corresponding to 1000 samples each of mining and nonmining classes are manually labeled. Nonmining areas include settlements, vegetation, clear water, barelands, and forests, and mining areas are digitized near settlements or vegetation and on different elevation forms. A random forest algorithm is fit on the labeled segments aligned with features consisting of Sentinel-2 spectral bands and COP-DEM for each block and applied to predict the unlabeled segments. This ML-assisted labeling process is followed by a meticulous and rigorous visual validation of the predicted segments. Misclassified segments are manually corrected by cross-checking historical high-resolution imagery from Google basemaps. In total, approximately 150 000 ASGM segments are labeled altogether. This comprehensive labeling effort provides a valuable dataset for advancing ASGM monitoring and research. Fig. 2 shows a sample patch and Fig. 3 presents a schematic overview of the workflow used to generate the ASGM labels.

C. Dataset Structure

A fishnet with grid dimension 128×128 pixels, corresponding to a ground distance of 1280×1280 m, is overlaid on the study area. Each grid is used to subset the coregistered

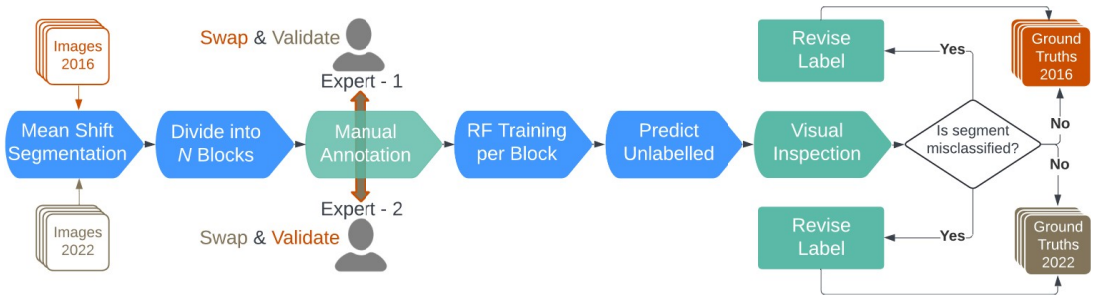

Fig. 3. Collaborative workflow for ASGM annotation and validation, where two annotators cross-validate each other's mapped data to ensure accuracy and reliability.

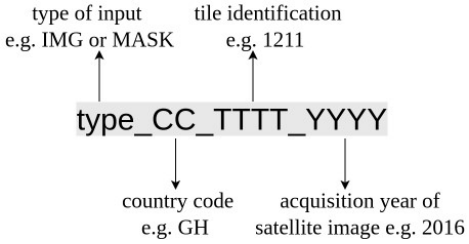

Fig. 4. Sample patches showing ASGM sites as observed from Sentinel-2 RGB, Sentinel-1 VV, and Copernicus DEM images.

composites of Sentinel-2, Sentinel-1, and COP-DEM independently for each year to produce an image of dimension $128 \times 128 \times 13$ bands and a corresponding binary mask of the same height and width. In total, 4270 patches were generated, with 2135 corresponding to each year. Each patch follows a naming conversion as shown in Fig. 4.

III. Experiments

SmallMinesDS is partitioned into training and validation subsets in a 70:30 ratio, using a histogram binning technique to ensure a balanced representation of mining and nonmining areas in both the sets. The task is formulated as a semantic segmentation problem, where each pixel in an input image is classified into one of two target classes: mining or nonmining. The rest of the section describes the models applied, evaluation metrics, and the results.

A. Models Used

Baseline: We used a random forest model with 300 estimators. This model required the input patches and masks to be flattened prior to training. To address the pixelwise class imbalance, the majority class (nonmining) was undersampled to match the number of samples in the minority class (mining).

U-Net: The U-Net architecture [25] using a ResNet-50 encoder [26] was implemented using the python library `segmentation_models_pytorch`. Two variants of the model—one initialized with ImageNet weights and another from scratch—were trained using a learning rate of 1×10^{-3}, reduced by a factor of 0.1 every ten epochs.

SAM-2: The second version of the segment anything model (SAM) [27] was accessed via Meta's publicly available checkpoints. Out of the four available options, `sam_2_hiera_small.pt` was chosen to balance fine-tuning speed and performance. Fine-tuning was carried out using a learning rate of 1×10^{-5} and weight decay of 4×10^{-5}.

Prithvi: The Prithvi-EO-2.0 backbone [28] was accessed through TerraTorch [29], a Python library based on PyTorch Lightning and TorchGeo, designed for flexible fine-tuning of geospatial FMs. The Prithvi foundation model is pretrained on the Harmonized Landsat Sentinel-2 (HLS) dataset. Fine-tuning was carried out using a learning rate of 1×10^{-3} and weight decay of 0.05.

Deep learning models were optimized using the binary cross-entropy loss [30] and the AdamW optimizer [31]. Due to the relatively lower occurrence of mining sites compared with the background class, a class weight in the ratio of 0.9 to 0.1 was used.

B. Evaluation Metrics

The models examined in our study were quantitatively evaluated using intersection over union (IoU), Sørensen–Dice coefficient (SDC), precision (P), and recall (R), such that

$$\text{IoU} = \frac{|A \cap B|}{|A \cup B|} \tag{1}$$

$$\text{SDC} = 2\frac{|A \cap B|}{|A|+|B|} \tag{2}$$

$$P = \frac{|A \cap B|}{|A|} \tag{3}$$

$$R = \frac{|A \cap B|}{|B|} \tag{4}$$

where A and B denote the prediction and ground-truth segmentation maps ranging between $[0-1]$, respectively. In binary segmentation, SDC is equal to F_1-score, which is the harmonic mean of precision and recall.

C. Results

Table I shows comparison of the performances of various models on the independent validation set considering only the target class (mining). Two band configurations were tested: RGB (three bands) and RGB+ (six bands). This selection was driven by the input data requirement of the pretrained and FMs. The Prithvi FMs attained an IoU of 75% similar to a pretrained U-Net but with better predictability of mining sites (87% against 80%) and a good balance between minimizing false positives and false negatives. No substantial difference was observed between the 300M and 600M Prithvi models,

TABLE I

QUANTITATIVE COMPARISON ON THE INDEPENDENT VALIDATION SET FOR THE MINING CLASS ONLY. PRETRAINED MODELS ARE INDICATED BY *. BOLD VALUES DENOTE THE BEST PERFORMANCE COLUMNWISE. EXPERIMENTS USING ONLY THE RED, GREEN, AND BLUE BANDS ARE REFERRED TO AS RGB, WHILE THOSE THAT ALSO INCORPORATE NARROW INFRARED AND THE TWO SHORT-WAVE INFRARED BANDS ARE REFERRED TO AS RGB+

Model	Band		Metric				Parameters	
	RGB	RGB+	IoU	Precision	Recall	SDC	Trainable	Total
Random Forest	✓		0.4109	0.9238	0.4253	0.5825	-	-
SAM-2*	✓		0.4261	0.7416	0.5004	0.5976	46M	46M
U-Net*	✓		0.7539	0.9278	0.8009	0.8597	9M	33M
Random Forest		✓	0.5027	0.9531	0.5155	0.6691	-	-
U-Net		✓	0.6513	**0.9642**	0.6675	0.7889	9M	33M
Prithvi-EO-2.0*		✓	**0.7579**	0.8558	0.8689	**0.8623**	15M	300M
Prithvi-EO-2.0*		✓	0.7560	0.8457	**0.8769**	0.8610	19M	600M

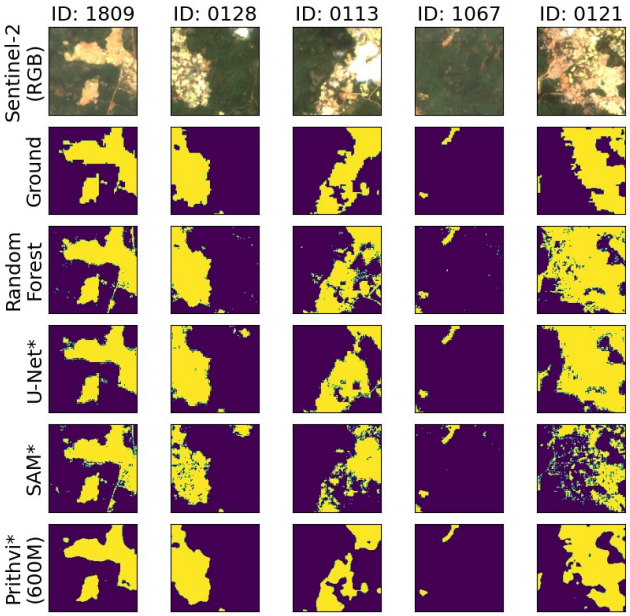

Fig. 5. Sample patches showing ASGM predictions in year 2016 for the baseline, pretrained/FMs. The positive class (mining) is shown in yellow.

indicating that they perform similarly. Random forest and SAM (although fine-tuned using point prompts on *SmallMinesDS*) showed significantly lower performance in the RGB configuration than the pretrained U-Net. Some studies suggest that text prompts and postprocessing using morphological operations can enhance semantic ambiguity in SAM [32]. When additional bands are augmented to RGB (referred to as RGB+), the performance of the random forest increases by around 20% in IoU, accuracy and recall. These results highlight the importance of extended spectral information for classical ML models. In contrast, the U-Net models did not exhibit the same behavior. The observed enhancement in U-Net* performance can primarily be attributed to its reliance on pretrained weights rather than the inclusion of additional spectral information [19].

From Fig. 5, Prithvi produces a better discrimination of mining segments with precise boundaries than the other models. Salt and pepper effects in the predictions are prominent in random forest [14] and SAM models. Where mining sites are close to settlements, such as in tile ID 0121, U-Net and random forest classified them as mining, exaggerating their footprints; however, the Prithvi model deciphered them better.

IV. POSSIBLE TASKS

While *SmallMinesDS* is primarily designed to facilitate the mapping of ASGM, it also contributes to the growing demand for high-quality and domain-diverse datasets to advance the development of FMs. Beyond its primary purpose, *SmallMinesDS* offers versatility across a range of research domains, particularly when supplemented with auxiliary datasets. Potential applications include the below.

1) *Environmental impact assessment*: Analyzing the spatiotemporal relationship between mining activities and vegetation cover, croplands, and water resources.
2) *Socioeconomic analysis*: Evaluating the effects of mining on population dynamics, shift in livelihood, and income levels within affected communities.
3) *Health and safety studies*: When paired with health-related datasets, *SmallMinesDS* can support the identification of mercury exposure pathways and investigation of mercury-induced health conditions.
4) *Land reclamation and restoration*: Supporting the monitoring and evaluation of land reclamation initiatives, as well as identifying mining sites that fail to adhere to sustainable practices.

Through its broad applicability, *SmallMinesDS* is an important resource for advancing interdisciplinary research and informing policy and decisions in sustainable mining, environmental protection, and community health.

V. LIMITATIONS

The development of *SmallMinesDS* is accompanied by limitations that warrant careful consideration. The segmentation process preceding the annotation of ASGM sites resulted in fine segments that were more precise than generalized. There is a tendency to find tiny spots (few pixels) of mining sites. Where there exist small islands of vegetation surrounded by ASGM sites, they may not be included in the mining class. The labels are also highly imbalanced, with small-scale mining areas constituting a disproportionately small fraction relative to the background class. Small patches of vegetation or linear features of polluted water located within mining sites may inadvertently be classified as part of the ASGM land use. In addition, pockets of cloud (occurring at low frequency in the 2016 image) in the southeastern portion of the study area were incorporated into the background class, as these regions do

not represent the target class of interest. Segments containing mixed land uses, where mining constitutes a relatively small proportion, have their labels assigned to the background class.

VI. Conclusion

In this study, we introduce *SmallMinesDS*, a novel and open-access multimodal dataset for mapping ASGM sites. This effort aims to bolster regulatory efforts for promoting sustainable and environmentally responsible practices within the ASGM sector by encouraging the development of innovative solutions that rely on remote sensing and artificial intelligence including the application of super-resolution techniques to potentially enhance the detection of small-scale gold mining activities [33]. Building on this work, future efforts will focus on expanding *SmallMinesDS* to cover other ASGM-prone regions in Africa, South America, and Asia. This expansion will enable the representation of cross-regional variations in ASGM practices, reflecting the diverse operational characteristics of mining activities globally and promoting case studies in transfer learning.

References

[1] *Global Mercury Assessment 2018*, UN Environ., Geneva, Switzerland, 2019.

[2] L. D. De Lacerda and W. Salomons, *Mercury from Gold and Silver Mining: A Chemical Time Bomb?*. Cham, Switzerland: Springer, 2012.

[3] L. J. Sonter, D. Herrera, D. J. Barrett, G. L. Galford, C. J. Moran, and B. S. Soares-Filho, "Mining drives extensive deforestation in the Brazilian Amazon," *Nature Commun.*, vol. 8, no. 1, p. 1013, Oct. 2017.

[4] P. Zhuang, B. Zou, N. Y. Li, and Z. A. Li, "Heavy metal contamination in soils and food crops around dabaoshan mine in Guangdong, China: Implication for human health," *Environ. Geochem. Health*, vol. 31, no. 6, pp. 707–715, Dec. 2009.

[5] *Environmental and Occupational Health Hazards Associated With Artisanal and Small-Scale Gold Mining*, World Health Org., Geneva, Switzerland, 2016.

[6] F. Aragon and J. P. Rud, "Mining, pollution and agricultural productivity: Evidence from Ghana," Dept. Econ., Simon Fraser Univ., Canada, Discuss. Paper dp12-08, Sep. 2012. [Online]. Available: http://www.sfu.ca/repec-econ/sfu/sfudps/dp12-08.pdf

[7] H. Gibb and K. G. O'Leary, "Mercury exposure and health impacts among individuals in the artisanal and small-scale gold mining community: A comprehensive review," *Environ. Health Perspect.*, vol. 122, no. 7, pp. 667–672, Jul. 2014.

[8] *On the Trail of African Gold: Quantifying Production and Trade to Combat Illicit Flows*, SWISSAID, Bern, Switzerland, May 2024.

[9] UNEP. (2013). *The Minamata Convention on Mercury*. [Online]. Available: https://www.mercuryconvention.org

[10] PlanetGOLD. (2019). *Making a World of Difference in Small-Scale Gold Mining*. Accessed: Nov. 29, 2024. [Online]. Available: https://www.planetgold.org

[11] G. Forkuor, T. Ullmann, and M. Griesbeck, "Mapping and monitoring small-scale mining activities in Ghana using Sentinel-1 time series (2015–2019)," *Remote Sens.*, vol. 12, no. 6, p. 911, Mar. 2020. [Online]. Available: https://www.mdpi.com/2072-4292/12/6/911

[12] A. Barenblitt et al., "The large footprint of small-scale artisanal gold mining in Ghana," *Sci. Total Environ.*, vol. 781, Aug. 2021, Art. no. 146644. [Online]. Available: https://www.sciencedirect.com/science/article/pii/S0048969721017125

[13] F. D. L. Lobo, P. W. M. Souza-Filho, E. M. L. D. M. Novo, F. M. Carlos, and C. C. F. Barbosa, "Mapping mining areas in the Brazilian Amazon using MSI/Sentinel-2 imagery (2017)," *Remote Sens.*, vol. 10, no. 8, p. 1178, Jul. 2018. [Online]. Available: https://www.mdpi.com/2072-4292/10/8/1178

[14] J. Gallwey, C. Robiati, J. Coggan, D. Vogt, and M. Eyre, "A Sentinel-2 based multispectral convolutional neural network for detecting artisanal small-scale mining in ghana: Applying deep learning to shallow mining," *Remote Sens. Environ.*, vol. 248, Oct. 2020, Art. no. 111970. [Online]. Available: https://www.sciencedirect.com/science/article/pii/S0034425720303400

[15] L. Tang and T. T. Werner, "Global mining footprint mapped from high-resolution satellite imagery," *Commun. Earth Environ.*, vol. 4, no. 1, p. 134, Apr. 2023.

[16] V. Maus et al., "A global-scale data set of mining areas," *Sci. Data*, vol. 7, no. 1, p. 289, Sep. 2020.

[17] W. Yu, S. Das, A. Rizaldy, X. Zhang, R. Gloaguen, and P. Ghamisi, "MineNet-CD: Global mining change detection dataset," in *Proc. IGARSS–IEEE Int. Geosci. Remote Sens. Symp.*, Jul. 2024, pp. 905–908.

[18] J. Jakubik et al., "Foundation models for generalist geospatial artificial intelligence," 2023, *arXiv:2310.18660*.

[19] A. Lacoste et al., "GEO-bench: Toward foundation models for Earth monitoring," in *Proc. Adv. Neural Inf. Process. Syst.*, vol. 36, 2023, pp. 51080–51093.

[20] Eur. Space Agency (ESA). *Copernicus Dem-Global and European Digital Elevation Model*. Accessed: Aug. 1, 2024. [Online]. Available: https://doi.org/10.5270/ESA-c5d3d65

[21] N. Gorelick, M. Hancher, M. Dixon, S. Ilyushchenko, D. Thau, and R. Moore, "Google Earth engine: Planetary-scale geospatial analysis for everyone," *Remote Sens. Environ.*, vol. 202, pp. 18–27, Dec. 2017, doi: 10.1016/j.rse.2017.06.031.

[22] Eur. Space Agency (ESA). (2016). *Copernicus Sentinel Data*. Accessed: Nov. 1, 2024. [Online]. Available: https://dataspace.copernicus.eu

[23] M. O. Source, M. McFarland, R. Emanuele, D. Morris, and T. Augspurger, 2022, "Microsoft/planetarycomputer, doi: 10.5281/zenodo.7261897.

[24] M. Grizonnet, J. Michel, V. Poughon, J. Inglada, M. Savinaud, and R. Cresson, "Orfeo ToolBox: Open source processing of remote sensing images," *Open Geospatial Data, Softw. Standards*, vol. 2, no. 1, p. 15, Jun. 2017.

[25] O. Ronneberger, P. Fischer, and T. Brox, "U-Net: Convolutional networks for biomedical image segmentation," 2015, *arXiv:1505.04597*.

[26] K. He, X. Zhang, S. Ren, and J. Sun, "Deep residual learning for image recognition," 2015, *arXiv:1512.03385*.

[27] N. Ravi et al., "SAM 2: Segment anything in images and videos," 2024, *arXiv:2408.00714*.

[28] D. Szwarcman et al., "Prithvi-EO-2.0: A versatile multi-temporal foundation model for Earth observation applications," 2024, *arXiv:2412.02732*.

[29] IBM. *Terratorch*. Accessed: Sep. 1, 2024. [Online]. Available: https://github.com/IBM/terratorch

[30] Z. Zhang and M. R. Sabuncu, "Generalized cross entropy loss for training deep neural networks with noisy labels," in *Proc. Adv. Neural Inf. Process. Syst.*, vol. 31, S. Bengio, H. Wallach, H. Larochelle, K. Grauman, N. Cesa-Bianchi, and R. Garnett, Eds., Dec. 2018, pp. 8792–8802. [Online]. Available: https://proceedings.neurips.cc/paperfiles/paper/2018/file/f2925f97bc13ad2852a7a551802feea0-Paper.pdf

[31] I. Loshchilov and F. Hutter, "Decoupled weight decay regularization," 2017, *arXiv:1711.05101*.

[32] R. Ibn Sultan, C. Li, H. Zhu, P. Khanduri, M. Brocanelli, and D. Zhu, "GeoSAM: Fine-tuning SAM with multi-modal prompts for mobility infrastructure segmentation," 2023, *arXiv:2311.11319*.

[33] J. Michel, J. Vinasco-Salinas, J. Inglada, and O. Hagolle, "SEN2VENμS, a dataset for the training of Sentinel-2 super-resolution algorithms," *Data*, vol. 7, no. 7, p. 96, Jul. 2022. [Online]. Available: https://www.mdpi.com/2306-5729/7/7/96